Titre: Title:	Terahertz tunable three-dimensional photonic jets
Auteurs: Authors:	Behrooz Rezaei, Babak Yahyapour, & Arash Darafsheh
Date:	2024
Type:	Article de revue / Article
Référence: Citation:	Rezaei, B., Yahyapour, B., & Darafsheh, A. (2024). Terahertz tunable three-dimensional photonic jets. Scientific Reports, 14, 16522 (14 pages). https://doi.org/10.1038/s41598-024-64158-6

Document en libre accès dans PolyPublie
Open Access document in PolyPublie

URL de PolyPublie: PolyPublie URL:	https://publications.polymtl.ca/58930/
Version:	Version officielle de l'éditeur / Published version Révisé par les pairs / Refereed
Conditions d'utilisation: Terms of Use:	Creative Commons Attribution 4.0 International (CC BY)

Document publié chez l'éditeur officiel
Document issued by the official publisher

Titre de la revue: Journal Title:	Scientific Reports (vol. 14)
Maison d'édition: Publisher:	Springer Nature
URL officiel: Official URL:	https://doi.org/10.1038/s41598-024-64158-6
Mention légale: Legal notice:	

scientific reports

OPEN

Terahertz tunable three-dimensional photonic jets

Behrooz Rezaei[1]✉, Babak Yahyapour[1,2] & Arash Darafsheh[3]

Highly localized electromagnetic field distributions near the "shadow-side" surface of certain transparent mesoscale bodies illuminated by light waves are called photonic jets. We demonstrated formation of three-dimensional (3D) tunable photonic jets in terahertz regime (terajets, TJs) by dielectric micro-objects -including spheres, cylinders, and cubes-coated with a bulk Dirac semimetal (BDS) layer, under uniform beam illumination. The optical characteristics of the produced TJs can be modulated dynamically through tuning the BDS layer's index of refraction via changing its Fermi energy. It is demonstrated that the Fermi energy of BDS layer has a significant impact on tuning the optical characteristics of the produced photonic jets for both TE and TM polarizations. A notable polarization dependency of the characteristics of the TJs was also observed. The impact of obliquity of the incident beam was studied as well and it was demonstrated that electromagnetic field distributions corresponding to asymmetric photonic jets can be formed in which the intensity at the focal region is preserved in a wide angular range which could find potential application in scanning devices. It was found that the maximum intensity of the TJ occurs at a non-trivial morphology-dependent source-angle.

Photonic nanojets (PNJs) were introduced as propagating narrow high-intensity electromagnetic beams generated at the "shadow-side" surface of dielectric micro-cylinders and -spheres with diameters larger than the incident plane-wave's wavelength[1–4]. The PNJ concept was later generalized to micro-objects with other morphologies[5], such as truncated spheres[6], spheroids[7], cuboids[8,9], axicones[10], gratings[11,12], and non-symmetrical objects[13], as well as other illuminating beams such as Gaussian[14] and Bessel[15] beams. PNJs have found potential applications in microscopy[16–19], spectroscopy[20], profilometry[21–27], photolithography[28,29], optical trapping[30], optical waveguides[31–34], and biophotonics[35–37]. Initially, PNJs were mainly investigated at the visible spectrum, but then they were extended to terahertz (THz) regime (named "terajets", TJs)[38–43] due to broad range of potential applications of the THz technology in medical and material sciences, as well as in communication, homeland security, and pharmaceutical industry[44–47]. Developing materials and structures for light manipulation in THz regime is an active area of research[48–51].

Optical characteristics of PNJs and TJs are governed by the index of refraction, geometry, and size of the generating micro-object[52–55] as well as the refractive index of the material around the micro-object[56] and properties of the incident light[2,57]. Refractive index can be modulated through incorporation of core–shell geometries[58,59], liquid crystals[60,61], temperature-sensitive vanadium oxide (VO_2) coating[62], and graphene coating[63,64] in dielectric micro-objects in order to produce tunable PNJs and TJs. Although these approaches allow dynamic control of the refractive index, they are associated with their own features and principles of operation, for example slow response time (typically on the order of milliseconds) in liquid crystals [65], control by precise change in the temperature in VO_2 (a phase change material), and the need to fabricate graphene with single-atom-layer thickness. In this context, ability to engineer materials with tunable refractive index in order to dynamically realize tunable TJs is appealing.

Dirac semimetals have been the subject of lots of recent research due to their ability in controlling the light propagation[66–73]. Bulk Dirac semimetals (BDSs) are topological materials and considered as 3D analogs of graphene due to their linear dispersion relation. The dielectric function of a BDS can be controlled dynamically through altering its Fermi energy by introducing an electric potential difference[74]. For electrically gating and controlling the Fermi energy, the electrolyte gating by means of ion gel could be utilized. The ion gel as a novel material with high conductivity has been used to electrically control the Fermi energy in layers of BDS[75]

[1]Department of Condensed Matter Physics, Faculty of Physics, University of Tabriz, Tabriz, Iran. [2]Department of Engineering Physics, Polytechnique Montreal, Montreal, QC, Canada. [3]Department of Radiation Oncology, Washington University School of Medicine in St. Louis, St. Louis, MO 63110, USA. ✉email: rezaeibhr@yahoo.com; b_rezaei@tabrizu.ac.ir

and chemical potential of graphene[76]. The properties of the ion gel makes it a suitable alternative for solid polymers and conventional media for electrical conduction applications such as gate material for use in field effect transistors. BDSs behave like a metal and a dielectric, when the frequency is below and above the Fermi energy, respectively. Their response time upon application of the external voltage is on the order of picoseconds (ps) to nanoseconds (ns)[77,78].

Very recently, we studied tunability of the optical properties of two-dimensional (2D) TJs produced by a BDS-coated dielectric rod[79]. In this paper, through numerical simulation, we demonstrate the formation of tunable TJs in BDS-coated 3D dielectric objects, including spheres, cylinders, and cubes, by optimizing their geometrical parameters and BDS layer's thickness. Optical properties of the generated TJs can be dynamically controlled via altering the Fermi energy of the BDS coating. The influence of the polarization of the incident light on the characteristics of the TJs is also studied. For an optimal value of the Fermi energy, the formation of TJs in those structures under an oblique incident beam is investigated. The obtained results demonstrate that the Fermi energy affects remarkably the optical properties of the TJs and by selecting an appropriate value of the Femi energy, the intensity of the TJ could be maintained over a wide angular range.

Geometry of the simulation

We performed finite-difference time-domain (FDTD) simulations in 3D using Lumerical software package (Lumerical Inc., Canada). Figure 1 shows the schematic of the proposed structures, a sphere, cylinder, and cube made of high-density polyethylene (HDPE) with refractive index $n_1 = 1.51$ at the THz frequency range[80], surrounded by air ($n_{bg} = 1$) and covered with a uniform BDS layer of thickness d_{DS} and index n_{DS}.

The quantitative key parameters of a typical PNJ or TJ are schematically presented in Fig. 1. Focal distance (FD) was defined as the distance from the proximal surface of the generating object to the focal point (locus of the maximum intensity) of the TJ. The TJ's transverse size, quantified as the full-width at half-maximum (FWHM) in the xy-plane along y-axis, was calculated at the focal point. The TJ's length was defined as the distance between proximal and distal $1/e$ contour of the intensity along the beam direction (x-axis).

The dielectric function, ε_{DS}, of the BDS can be written as[67]:
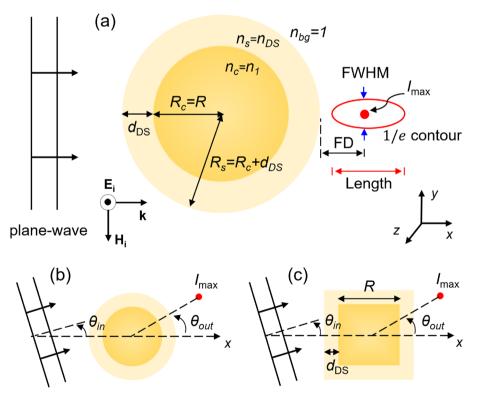

Figure 1. Schematic of the simulation geometry. A uniform beam, propagating along the x-axis, impinges upon a sphere (radius R), a cylinder (radius R and height h), and a cube (length R) with refractive index n_1 coated with a BDS with thickness d_{DS} and index n_{DS}. (**a**) Terajet characteristics include focal distance (calculated from the proximal surface of the particle to the locus of the maximum intensity), beam FWHM in xy plane, TJ length (measured as the distance between distal to proximal $1/e$ intensity contour along the direction of the TJ, i.e. x-axis), and the maximum relative intensity. Geometry of oblique incident for a (**b**) sphere/cylinder and (**c**) cube. In the core–shell structure shown in panel (**a**), n_c (R_c) and n_s (R_s) represent the refractive indices (radii) of the core and shell, respectively. Drawings are not to scale.

$$\varepsilon_{DS}(f, E_f) = \varepsilon_b + i \frac{\sigma_{DS}(f, E_f)}{2\pi f \varepsilon_0} = \varepsilon_b - \frac{\mathrm{Im}\{\sigma_{DS}(f, E_F)\}}{2\pi f \varepsilon_0} + i \frac{\mathrm{Re}\{\sigma_{DS}(f, E_F)\}}{2\pi f \varepsilon_0} \tag{1a}$$

in which f is the frequency of the incident wave, ε_b is the background's effective dielectric constant, ε_0 is the permittivity of vacuum, $i = \sqrt{-1}$, and $\sigma_{DS}(f, E_f)$ represents the BDS's conductivity at a given frequency and Fermi Energy (E_f). The following equations give the complex optical conductivity of the BDS [67]:

$$\mathrm{Re}\{\sigma_{DS}(f, E_F)\} = \frac{e^2 g k_F f}{12 E_F} \frac{\sinh\left(\frac{hf}{2k_B T}\right)}{\cosh\left(\frac{E_F}{k_B T}\right) + \cosh\left(\frac{hf}{2k_B T}\right)} \tag{1b}$$

$$\mathrm{Im}\{\sigma_{DS}(f, E_F)\} = \frac{e^2 g k_F}{12\pi h} \left[\frac{4 E_F}{hf}\left(1 + \frac{\pi^2}{3}\left(\frac{k_B T}{E_F}\right)^2\right) + \frac{8hf}{E_F} \int_0^{\varepsilon_c = 3} \left(\frac{\frac{\sinh\left(\frac{\varepsilon E_f}{k_B T}\right)}{\cosh\left(\frac{E_F}{k_B T}\right) + \cosh\left(\frac{\varepsilon E_f}{k_B T}\right)} - \frac{\sinh\left(\frac{hf}{2k_B T}\right)}{\cosh\left(\frac{E_F}{k_B T}\right) + \cosh\left(\frac{hf}{2k_B T}\right)}}{\left(\frac{hf}{E_f}\right)^2 - 4\varepsilon^2} \right) \varepsilon \, d\varepsilon \right] \tag{1c}$$

in which $k_F = E_F/\hbar v_F$ is the Fermi momentum, $v_F = 10^6$ m/s is the Fermi velocity, $\varepsilon = E/E_F$, $\varepsilon_c = E_c/E_F$, E_c is the cut off energy above which the dispersion relation of the BDS becomes non-linear ($\varepsilon_c = 3$ is our case), and $T = 300$ K is the temperature. Symbols k_B, e, $\hbar$, and g represent the Boltzmann constant, an electron's charge, the reduced Planck constant, and the degeneracy factor ($g = 4$), respectively.

A uniform beam propagating along the x-axis, with unit amplitude, whose electric field oscillates along the i) z-axis (TE) and ii) y-axis (TM) was incident upon the proposed structures to investigate the dependency of the produced TJs on the polarization of the light source. The computational mesh size was $\Delta x = \Delta y = \Delta z = 0.3$ μm ($\sim \lambda/140$-$\lambda/100$) to secure converging results. The perfectly matched layers (PMLs) boundary condition (34-μm-thick) were employed around the simulation region to prevent spurious reflection [81]. The incident uniform beam had a finite size encompassing the whole cross-sectional area of the object; its size along y-axis (z-axis) is 1200.3 μm (2201.4 μm) for sphere, 694.4 μm (680.9 μm) for cylinder, and 481.3 μm (691.8 μm) for the cube. The distance between the center of the source and center of the all dielectric sphere, cylinder, and the cube objects is 30 μm. Each run took about 8–9 h, 4–5 h, and 4–5 h for a sphere, cylinder, and cube, respectively, in our system with 64 GB RAM.

We numerically investigate the ability of the proposed BDS-coated dielectric objects (sphere, cubic and cylinder) to produce TJs, and control their optical properties by altering the BDS layer's Fermi energy at room temperature. The BDS layer is considered to have similar properties to Cd_3As_2 (cadmium arsenide) and Na_3Bi (trisodium bismuthide) with $\varepsilon_b = 12$ and $g = 4$ [67]. In contrast to 2D Dirac fermions in graphene or on the surface of 3D topological insulators, topological DSs possess 3D Dirac fermions in the bulk. Cd_3As_2 is a 3D DS material with separated Dirac points and linear energy dispersion in momentum space. It is a tetragonal material with space group I41/acd and lattice constants of $a = b = 1.26$ nm and $c \approx 2.54$ nm, which remains nearly cubic ($2a = 2b \approx c$) [82]. This cell contains 96 cadmium atoms and 64 arsenic atoms with two cadmium vacancies. The Dirac equation describes the massless electrons in Cd_3As_2, suggesting a conical band that has twice degenerated due to spin. The crystal structure of Na_3Bi, as a topological DS, is a body-centered tetragonal with space group of P4/mmm. The electronic band structure measurements and calculations of Na_3Bi DS show a cone-shape with linear dispersion [68]. The lattice constants of Na_3Bi at the ground state are $a = 3.4116 \text{Å}$ and $c = 4.9530 \text{Å}$ [83].

Cd_3As_2, as a 3D BDS, has attracted research interests due to its chemical stability and extraordinary optical response[84]. It has been fabricated in thin films and at nanoscale through different techniques, including physical vapor deposition (PVD)[85], pulse laser deposition (PLD)[86], molecular beam epitaxy (MBE)[87], chemical vapor deposition (CVD) [88], and self-selecting vapor growth (SSVG)[82].

The complex index of refraction of a non-magnetic medium is obtained through $\tilde{n}(\omega) = \sqrt{\varepsilon_{DS}(\omega)}$. The behavior of the real and imaginary index of refraction of the considered BDS versus the Fermi energy ($E_F = 5$–60 meV) are plotted in Fig. 2 at different frequencies (6–10 THz). It can be seen that as the frequency decreases, the amount of change in the refractive index (dynamic range) over the range of Fermi energies increases, indicating higher degree of tunability of the produced TJs. However, at 6 THz, the real part of the index drops quickly to low values close to and smaller than unity. Hence, $f = 7$ THz ($\lambda = 42.83$ μm) which maintains a reasonably high index while providing the highest dynamic range was selected for all simulations in this work. The real part (n_r) of the index decreases gradually with Fermi energy up to a certain energy beyond which it drops suddenly. The imaginary part (n_i) of the refractive index decrease as the Fermi energy increases up to a certain energy beyond which it starts to increase. We chose $E_F = 10$ meV as the lower end at which $n_r = 2.669$ and $n_i = 0.071$. At 7 THz and for $E_F > 55$ meV, the real part of the index reaches unity, so $E_F = 55$ meV was selected as the higher end at which $n_r = 1.187$ and $n_i = 0.066$. Due to a relatively low n_i, the absorption associated with the BDS layer will be low in the selected Fermi energy range ($E_F \in ^{10-55}$).

It should be mentioned that in practice the E_F and consequently the BDS's index can be modulated dynamically through applying a voltage[89–92], or by an alkaline surface doping [68,93]. In this way, the propagation of light can be modulated by the BDS-coated objects, affecting the generated TJs' characteristics.

In order to demonstrate the formation of tunable 3D TJs, we considered three cases: (i) a BDS-coated dielectric sphere with radius $R = 500$ μm ($\sim 11.7\lambda$) and thickness of the BDS layer $d_{DS} = 1.5$ μm ($\sim 0.035\lambda$); (ii) a cylinder with radius $R = 300$ μm ($\sim 7\lambda$), height $h = 180$ μm ($\sim 4.2\lambda$), and thickness of the BDS layer $d_{DS} = 1.5$ μm;
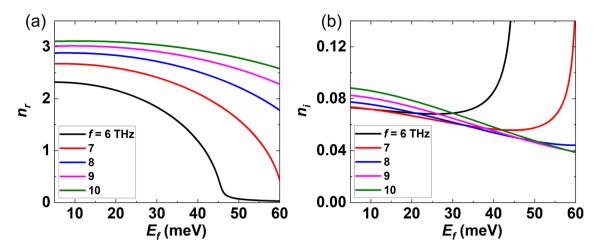
Figure 2. The index of refraction of a BDS, mimicking Na_3Bi or Cd_3As_2, versus E_F at several THz frequencies at room temperature: (**a**) real and (**b**) imaginary part.

(iii) a cube with side length $R = 300$ μm and thickness of the BDS layer $d_{DS} = 1.5$ μm. The thickness of the BDS layer was kept small in all cases to minimize the absorption. The object's size for each case was obtained through simulating objects with sizes in the range 2λ up to 25λ, where λ is the wavelength, with 0.1λ increments and selecting the size that produced the highest intensity TJ. This is the size range over which production of photonic jets is more efficient [53]. Next, the BDS layer with different thicknesses between 0.5–2 μm, with 0.1 μm increments, was added and the optimum thickness was selected. Here, there is a trade-off between refractive power of the layer and its absorption imposed by the imaginary component of the refractive index.

Next, we studied the impact of the obliquity of the incident uniform beam on the TJ formation in the abovementioned cases. Figure 1b,c show the geometry of the oblique incident case on a sphere/cylinder and a cube, respectively. The input source angle was defined as the rotation angle of the source along x-axis as represented by θ_{in} in Fig. 1b,c. The emergence angle of the TJ was defined as the angle between the x-axis and the line passing through the location of the maximum intensity outside of the object and the center of the object as shown by θ_{out} in Fig. 1b,c. Other parameters of the simulation remained unchanged.

Results and discussions

The distribution of the electric field of the TJs produced by the BDS-coated sphere at Fermi energies of $E_F = 10$ meV and $E_F = 55$ meV, for TE-polarized incident wave, are presented in Fig. 3a,b, respectively. The corresponding results for the TM-polarized case are presented in Fig. 3c,d, respectively. The modulation of the characteristics of the produced TJs, realized through changing the BDS layer's Fermi energy, are presented in Fig. 3e,f. Since the intensity is proportional to the second power of the electric field distribution, in order to calculate the TJ's FWHM, the location of the maximum intensity is identified first. Next the intensity profile along a line parallel to the y-axis passing through the location of the maximum intensity is obtained. We observed a decreasing (increasing) trend in FD and length (intensity and FWHM) of the TJs as the Fermi energy increases. For example, for the TM (TE) incident wave, the FD decreased from 68.4 (74.7) μm to 62.8 (63.2) μm when the E_F of the BDS layer was increased from 10 to 55 meV, providing 5.6 (11.5) μm dynamic range. Also, within the same Fermi energy range, the enhancement in intensity of the TJ was increased from 313.5 (332.5) to 572.9 (624.4) for the TM (TE) case. The FWHM decreased from 35.4 (32.6) μm to 31.23 (26.4) μm while the TJ length increased from 78.4 (84.6) μm to 88.9 (97.2) μm in which the corresponding amounts of tuning were 4.17 (6.2) μm and 10.5 (12.6) μm, respectively. It can be seen that the TE case provides more dynamic range for the tuning compared to the TM case. The focal distance and TJs are longer, more intense, with smaller FWHM in TE cases compared to the TM cases. It has been suggested that TM polarization generates wider PNJs compared to the TE polarization due to longitudinal component of the TM-polarized incident light[94].

The distribution of the electric field of the TJs generated by the cylinder at $E_F = 10$ meV and $E_F = 55$ meV, for TE polarized incident wave, are shown in Fig. 4a,b, respectively. The corresponding cases for the TM-polarized case are presented in Fig. 4c,d, respectively. The plots of the TJ's FD and intensity, as a function of E_F, are presented in Fig. 4). The plots of the TJ's FWHM and length, as a function of E_F, are presented in Fig. 4f. It can be seen that the optical characteristics of the produced TJs follow a similar trend as in the corresponding sphere cases in terms of the Fermi energy. However, the sphere provided TJs with an order of magnitude more intensity. The intensity enhancement of the TJ varied between 28.9 (27.2) and 40.75 (51.7) for TM (TE) case. The amount of tuning for FD is 9 μm (10 μm), which varies from 67.5 μm (73.2 μm) to 58.5 μm (63.2 μm) for the TM (TE) case. The FWHM varied between 29.4 μm (21.3 μm) and 32.4 μm (27.1 μm) for TM (TE) case. The TJ length varied between 94 μm (84.6 μm) and 112.7 μm (132.4 μm). The TE case provided more dynamic range for the tunability compared to the TM case.

Using geometrical optics paraxial approximation [18], we can calculate the focal distance of a core–shell system with circular cross-section with the core and shell radii of R_c and R_s and refractive indices of n_c and n_s, respectively, as:
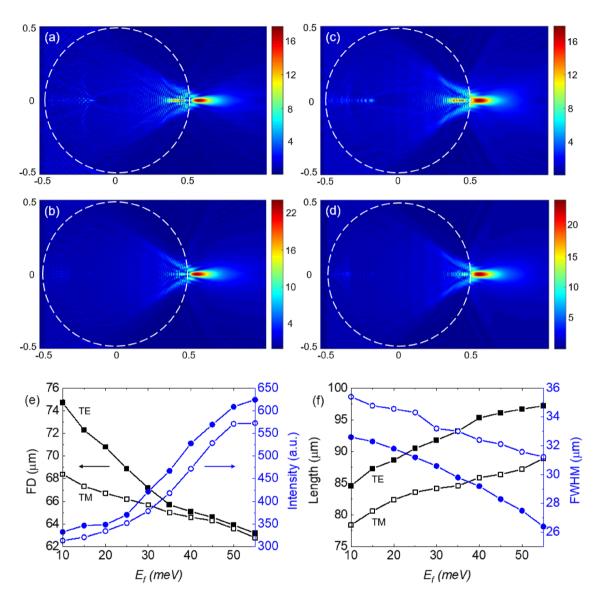
Figure 3. The electric field distribution inside and around a BDS-coated dielectric sphere with $R = 500$ μm and $d_{DS} = 1.5$ μm at $T = 300$ K for (**a**) $E_F = 10$ meV (TE), (**b**) $E_F = 55$ meV (TE), (**c**) $E_F = 10$ meV (TM), and (**d**) $E_F = 55$ meV (TM). (**e**) TJ's calculated FD (square symbols) and intensity (circle symbols) versus E_F. (**f**) TJ's length (square symbol) and FWHM (circle symbol) versus E_F. Hollow (solid) symbols correspond to TM (TE) polarization of the incident uniform beam.

$$FD = \frac{R_s(2R_s n_c - 2R_c n_c - 2R_s n_s + R_c n_c n_s)}{2(-R_s n_c + R_c n_c + R_s n_s - R_c n_c n_s)} \qquad (2)$$

For our core–shell spheres with $R_c = 500$ μm and $R_s = 501.5$ μm, we have $FD = 242.8$ μm and 239.7 μm at $E_F = 10$ meV and $E_F = 55$ meV, respectively. For the same sphere without the shell, the FD is 240.2 μm. In our core–shell structures composed of concentric spheres and co-axial cylinders, the core due to its significantly larger size influences the focusing more than the shell does. Obviously, we do not expect to accurately calculate the characteristics of mesoscale objects using geometrical optics. However, it is interesting to note that the trend is in agreement with the FDTD simulation results. As the shell index decreases with the increase of the E_f, the FD decreases. TJ formation is a complex interplay of the incoming, refracted, and diffracted waves inside and around the micro-object. Generally, smaller spheres and cylinders produce PJs closer to the distal interface, i.e. shorter FD, with smaller FWHM; also, higher refractive index of the core, would lead to shorter FD and smaller FWHM of the produced PJ [2]. In principle, these parameters can be further exploited to optimize the TJs.

In our previous work for 2D cases, we observed intensity enhancement factors in the range of ~ 9.5–22, here for the 3D cylinders the intensity enhancement factor is ~ 41–52. In addition to the refracted waves and diffracted waves at the periphery of the cylinder, the diffracted waves from the sides also contribute to the focal point's intensity in the 3D case.
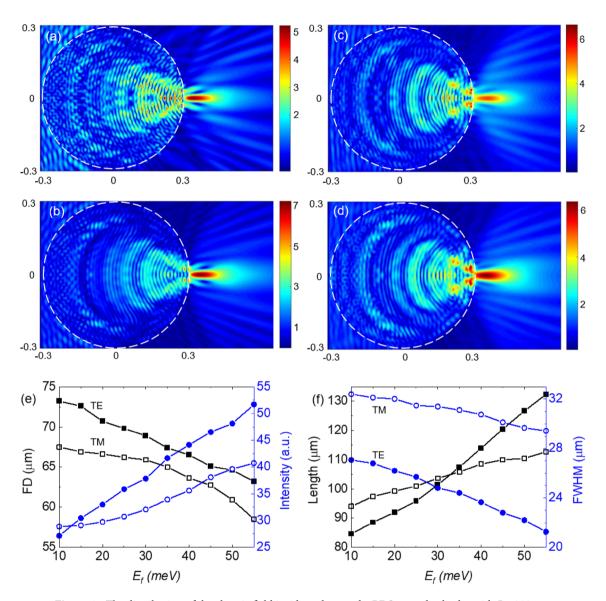
Figure 4. The distribution of the electric field inside and around a BDS-coated cylinder with $R = 300$ μm and $d_{DS} = 1.5$ μm at $T = 300$ K for (**a**) $E_F = 10$ meV (TE), (**b**) $E_F = 55$ meV (TE), (**c**) $E_F = 10$ meV (TM), and (**d**) $E_F = 55$ meV (TM). (**e**) TJ's FD (square symbols) and intensity (circle symbols) versus E_F. (**f**) TJ's calculated length (square symbols) and FWHM (circle symbols) versus E_F. Hollow (solid) symbols correspond to TM (TE) polarization of the incident uniform beam.

Figure 5 shows how the optical properties of a TJ produced by a cube changes as the E_F of the BDS coating changes. The distribution of the electric field of the TJs, for the TE-polarized incident wave, at $E_F = 10$ meV and $E_F = 55$ meV are shown in Fig. 5a,b, respectively. The quantitative properties of the TJs for the TM-polarized light source as a function of the E_F are presented in Fig. 5c,d showing a similar trend as in the sphere and cylinder cases. However, the intensity in the cube-generated TJs is less than those produced by cylinders/spheres and the focal distance is longer due to the weaker focusing effect in the cube. The intensity enhancement of the TJ varied between 6.2 (6.4) and 8.6 (9.2) for TM (TE) case. The FD varies between 436.5 (458) μm and 397.5 (417) μm corresponding to 39 (41) μm tuning for TM (TE) case. Within the same Fermi energy, the FWHM with a tuning of 4.2 μm (5.6) reduces from 62.3 (56.4) μm to 58.1 (50.8) μm, while the length of TJ with a tuning of 49.4 (40) μm increased from 320 (342) μm to 369.4 (382) μm for TM (TE) case. The TE case provided more dynamic range for the tunability compared to the TM case for the intensity, focal distance, and the spot size. The TJ length showed more dynamic range for the TM case compared to the TE case.

In most of the cases, the focal distance and TJs are longer, more intense with smaller FWHM in TE cases compared to the TM cases. When comparing the findings for all 3D TJs, the highest tuning of the intensity is attained for spheres, while the tuning of the TJ's length is more noticeable for the cube. In all cases, as the E_f increases, the intensity of the TJ increases. It can be in part explained by the fact that since the index of the BDS coating decreases as E_f increases, the Fresnel losses at each interface decrease which increases the photon fluence at the focal point. The intensity of the TJ is highest for the sphere due to its extended curved boundary compared to the cylinder and cube that provides high photon fluence at the focal point. The TJ lengths are longer in the
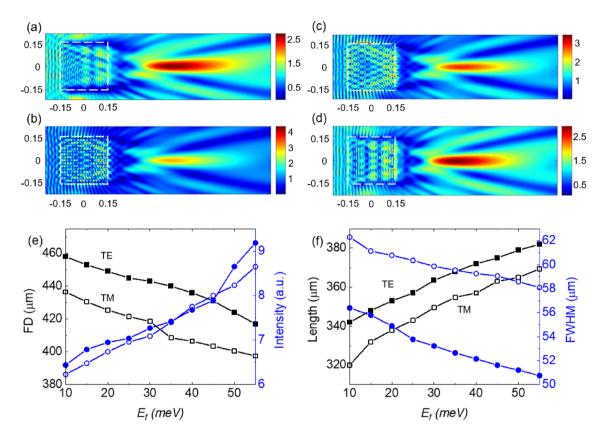
Figure 5. Distribution of the electric field distribution around and inside a BDS-coated cube with $R = 300$ μm and $d_{DS} = 1.5$ μm at $T = 300$ K for (**a**) $E_F = 10$ meV (TE), (**b**) $E_F = 55$ meV (TE), (**c**) $E_F = 10$ meV (TM), and (**d**) $E_F = 55$ meV (TM). (**e**) Plot of FD (square symbols) and intensity (circle symbols) vs. E_F. (**f**) TJ's length (square) and FWHM (circle) versuss E_F. Hollow (solid) symbols correspond to TM (TE) polarization of the light source.

cubes (cylinders) than those in the cylinders (spheres). A quick convergence of the Poynting vector around the focal spot would produce more intense TJs with shorter length [95]. However, when the Poynting vector is less diverging and remains parallel near the focal spot, the TJ is more elongated with longer FD as in the cube case.

Figure 6 shows the TJ's electric field distribution (for $E_F = 55$ meV) in the beam's eye-view, i.e. yz-plane encompassing the locus of maximum intensity. The TJ's FWHM along the y-axis is what we have reported so far.
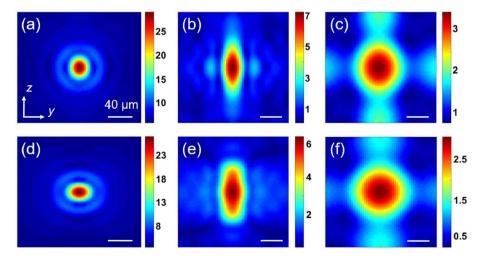

Figure 6. Distribution of the electric field inside and around a BDS-coated (**a, d**) sphere ($R = 500$ μm and $d_{DS} = 1.5$ μm), (**b, e**) cylinder ($R = 300$ μm and $d_{DS} = 1.5$ μm), and (**c, f**) cube ($R = 300$ μm and $d_{DS} = 1.5$ μm) at $T = 300$ K and $E_F = 55$ meV. Polarization of the incident wave is along the (**a–c**) z-axis (TE) and (**d–f**) y-axis (TM). Scale bars are 40 μm.

The TJ's FWHM was calculated along the z-axis as well for these cases presented in Fig. 6. The FWHM values along y-axis (z-axis) are 31.2 (25.7), 29.4 (69.7), and 58.1 (62.4) μm for the sphere, cylinder, and cube, respectively, under normal incidence and TM polarization of the uniform beam. The corresponding values for the TE case are 26.4 (32.8), 21.3 (49.3), and 50.8 (66) μm. It can be seen that the TJ distribution is not totally symmetric, a consequence of vectorial nature of the incident uniform beam. According to Richards and Wolf diffraction theory [96], under high numerical aperture focus, the intensity profile of the focal spot would be elongated along the direction of the polarization. Here we see that effect in the produced TJs; for TE (TM) case elongation of the TJ can be seen along z-axis (y-axis).

Next, we analyzed the optical properties of BDS-coated dielectric objects under oblique incidence to verify the robustness of the produced TJs at various angles of the incident beam. We found that the intensity of the TJ was maximum at $E_F = 55$ meV within the range of studied Fermi energies. Figure 7a–d illustrate the simulation results of electric field distribution in the xy-plane for source rotation angles of 5°, 25°, 40°, and 60° for the TE case. The corresponding results for the TM case are presented in Fig. 7e–h. When the source angle was altered, the TJ was deflected, and the intensity at the focused region was maintained over a large angular range, demonstrating the micro-object's ability to work as a wide-scanning TJ-focusing lens. When the angle of the incident uniform beam was varied, the numerical results for deflection angle of the TJ produced by the sphere is presented in Fig. 7i. The intensity as a function of the rotation angle of the incident uniform beam is shown in Fig. 7j. It should be noted that the uniform beam source was rotated along the x-axis which caused the asymmetric appearance of the TJs. It should be noted that the asymmetry is caused by the finite size of the incident uniform beam that leads to partial illumination of the object. Interestingly, it can be seen that the maximum intensity of the TJ occurs at ~ 5° source rotation angle, not necessarily at normal incidence. Introduction of an asymmetric optical path length along the optical axis due to the obliquity of the incident beam produces an asymmetric TJ as a result of difference between phase velocity and the interference of the waves inside the particle.

The simulation results for the cylinder case at $E_F = 55$ meV are presented in Fig. 8 indicating how the TJ is deflected by changing the source rotation angle. Figure 8a–d represent the electric field distribution in xy-plane
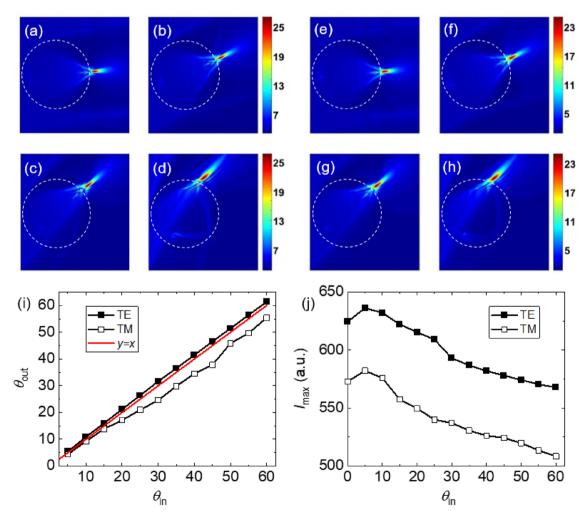

Figure 7. (**a–d**) The electric field distributions of the TJ formed by a BDS-coated dielectric sphere with $R = 500$ μm and $d_{DS} = 1.5$ μm at Fermi energy of $E_F = 55$ meV for input angles of (**a**) 5°, (**b**) 25°, (**c**) 40° and (**d**) 60° for the TE case. (**e–h**) The TM counterparts of (**a–d**). The dashed circles show the boundary of the sphere. (**i, j**) The emergence angle and intensity of the TJ, respectively, as a function of the uniform beam rotation angle.
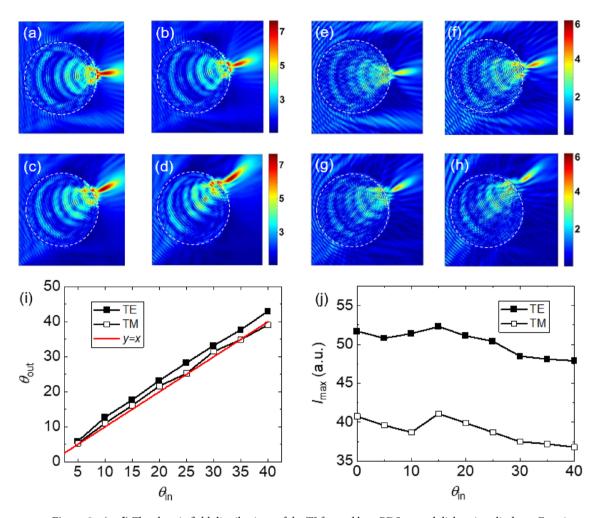
Figure 8. (**a–d**) The electric field distributions of the TJ formed by a BDS-coated dielectric cylinder at Fermi energy of $E_F = 55$ meV for source rotation angles of (**b**) 5°, (**c**) 15°, (**d**) 25°, and (**e**) 40° for the TE case. (**e–h**) The TM counterparts of (**a–d**). The dashed circles represent the boundary of the cylinder. (**i, j**) The emergence angle and intensity of the TJ, respectively, as a function of the uniform beam rotation angle.

for input angles of 5°, 15°, 25°, and 40° for TE case. The corresponding results for the TM case are presented in Fig. 8e–h. Figure 8i shows the dependency of the deflected angle of the TJ versus the source rotation angle. The intensity as a function of the source rotation angle is shown Fig. 8j. The observed asymmetry in the TJ shape is due to the fact that the source was rotated along the x-axis. Similar to the sphere case, it can be seen that the maximum intensity of the TJ occurs at a non-trivial source rotation angle, here at ∼15° source rotation angle.

The simulation results for the 3D BDS-coated cube at $E_F = 55$ meV is shown in Fig. 9. Figure 9a–d show the electric field distribution for input angles of 5°, 10°, 20°, and 35° for the TE case. The corresponding results for the TM case are presented in Fig. 9e–h. Figure 9i,j show the relationship between the output angle and intensity as a function of the input angle. Similar to the sphere and cube cases, it can be seen that the maximum intensity of the TJ occurs at a morphology-dependent source rotation angle, here at ∼10°.

It can be seen in Figs. 7, 8, 9 that the exit angle of the TJs in the sphere and cylinder cases follow a somewhat symmetric trend with respect to the incident angle due to the inherent circular symmetry of the producing micro-object. However, the asymmetry between θ_{in} and θ_{out} in the cube case is mostly stems from the lack of rotational symmetry of the cube compared to the sphere/cylinder.

A list of PJ characteristics produced using different objects at different wavelengths is provided in Table 1. These parameters should scale with the wavelength following Maxwell's equations. A distinct feature of the current work with the majority of the previous works is that the PJs are dynamically tunable. Depending on the
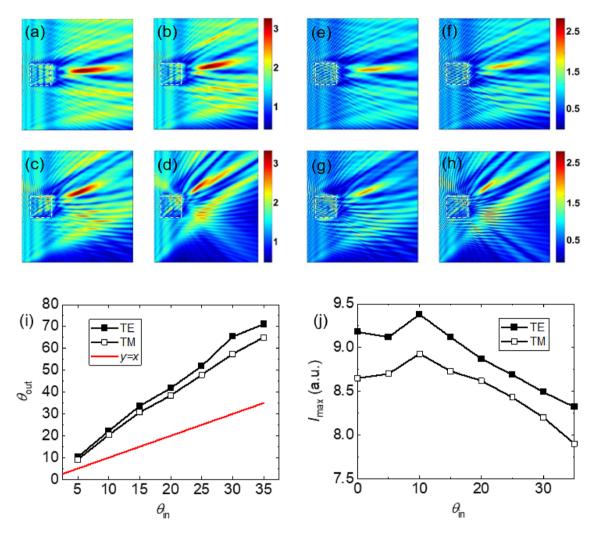
Figure 9. (**a**–**d**) The electric field distributions of the TJ formed by a BDS-coated dielectric cube with $R = 300$ μm and $d_{DS} = 1.5$ μm at Fermi energy of $E_F = 55$ meV for source rotation angles of (**a**) 5°, (**b**) 10°, (**c**) 20°, and (**d**) 35° for the TE case. (**e**–**h**) The TM counterparts of (a-d). The dashed squares represent the boundary of the cube. (**i**, **j**) The output angle and intensity of the TJ, respectively, as a function of the uniform beam rotation angle.

application, operation wavelength, and choice of available materials, an ad hoc simulation must be performed to select the optimum PJ-producing geometry.

The proposed structures made of Cd_3As_2 may be associated with certain considerations. For example, due to the high toxicity of Cd and As, extra caution is required in handling of these elements during the synthesis. Although various fabrication methods for Cd_3As_2 have been reported, a high-yield cost-effective large-scale fabrication method has not been established yet, unlike the case for semiconductor chip fabrication.

Conclusions

Through FDTD numerical simulation, we demonstrated formation of tunable 3D photonic jets in terahertz spectral domain (terajets, TJs) by dielectric spheres, cubes, and cylinders coated with a BDS layer. The dependency of the TJ's main characteristics (FD, FWHM, intensity, and length) on the BDS's Fermi energy and incident uniform beam's polarization was explored for each case. Polarization of the illuminating light was found to play an important role on TJ characteristics. Simulation of the TJs under oblique incident demonstrated formation of asymmetric focused beams with the maximum intensity of the TJs at a non-trivial morphology-dependent source-angle.

Shape	Wavelength (λ) (µm)	Size (D/λ)	Index contrast	FWHM/λ	Intensity enhancement factor (I_{max}/I_0)	Jet length/λ	Tunable	References
DS-coated 3D sphere	42.83	23.34	$n_c = 1.51$	0.76–0.62 (TE) 0.83–0.73 (TM)	332.5–624.4 (TE) 313.5–572.9 (TM)	1.97–2.27 (TE) 1.83–2.07 (TM)	Yes	This work
DS-coated 3D cylinder	42.83	~4.2 to 14	$n_c = 1.51$	0.63–0.50 (TE) 0.76–0.69 (TM)	27.2–51.7 (TE) 28.9–40.75 (TM)	1.97–3.09 (TE) 2.19–2.63 (TM)	Yes	This work
DS-coated 3D cube	42.83	7	$n_c = 1.51$	1.32–1.19 (TE) 1.45–1.36 (TM)	6.4–9.2 (TE) 6.2–8.6 (TM)	7.98–9.92 (TE) 7.47–8.62 (TM)	Yes	This work
DS-coated 2D cylinder	37.47	19.2	$n_c = 1.44$	~1.03 to 0.56	8.8–17.5	~9.3 to 6.2	Yes	[79]
DS-coated 2D cylinder	37.47	30.4	$n_c = 1.44$	~0.93 to 0.67	9.45–22.4	~5.84 to 3.82	Yes	[79]
DS-coated 2D cylinder	33.33	21.6	$n_c = 1.44$	~0.97 to 0.7	11.1–20.1	~5.3 to 3	Yes	[79]
DS-coated 2D cylinder	42.83	23.4	$n_c = 1.44$	~0.7 to 0.65	15.9–22.4	~7.5 to 8.4	Yes	[79]
Circular LC core–shell	0.676	5	1.738	~0.45 to 0.34	~0.7 to 1	~3.6 to 1.8	Yes	[61]
Elliptical LC core–shell	0.676	5	1.738	~0.7–0.32	~0.3 to 1	~10.4 to 1	Yes	[61]
VO$_2$-coated sphere	0.8	~6.34	1.5	0.5375–0.4625	22.7	N/R	Yes	[62]
Cylinder	0.2–0.5	10–33.33	1.7–1.75	0.5–0.66	N/R	1.6–3.33	No	[1]
Sphere	0.4	2.5–20	1.59	0.325–525	N/R	N/R	No	[54]
Sphere	0.9	~3.5 to 4.4	1.49	0.41–0.78	~8–17	2.3–9.3	No	[14]
Sphere	0.532	~10.8	1.5	~0.5	~200	N/R	No	[97]
Axicon	1	~6 to 7	1.5	0.3	~50	N/R	No	[98]
Axicon	0.532	1–6	1.46	~0.45 to 0.79	~20 to 40	~3.5 to 5.5	No	[13]
Axicon	0.532	~1.9 to 5.6	1.5	~0.45 to 0.79	Up to 40	Up to 5.5	No	[10]
Cube	3000	1.2	1.75	<0.4	~15	N/R	No	[9]
Cube	3000	1.2	1.41	0.46	~10	N/R	No	[9]
Cuboid	0.532	0.5–6	1.46	~0.43 to 1.75	N/R	Up to 25	No	[8]
Cuboid (reflection)	Scaled	0.2–1	1.46	~0.4	Up to 17	1.08	No	[39]
Cuboid array	8570	1	1.46	0.43–05	N/R	~2	No	[38]
Triangular prism	4	~5.5 to 20	1.46	1.8	Up to 9	N/R	No	[99]
Triangular prism	4	~4.4 to 20	1.56	0.3	Up to 8.9	N/R	No	[99]
Triangular prism	4	~3.75 to 20	1.8	0.375	Up to 9	N/R	No	[99]
Core–shell sphere	0.532	5.64	$n_c = 1.6$, $n_s = 1.84$	~0.56	~28	~2.3	No	[10]
Core–shell sphere	100	5	$n_c = 1.33$, $n_s = 1.46$	0.37–0.91	53.6–261	N/R	No	[100]
Hemispheric shell	0.4	6.25–12.5	1.5	0.455	~150	4.25	No	[101]
Hemispheric shell	1	2.5–5	1.5	0.584	~45	4.3	No	[101]
Immersed core–shell hemisphere	0.365	~24.6	$n_c = 1.44$, $n_s = 1.57$	~0.8 to 1.15	~60 to 200	~8–23	No	[102]
Immersed flat-top hemisphere	0.325–0.4	~24.6	1.57	~0.89 to 1	~70 to 125	~14 to 31.9	No	[102]
Square steps	0.633	~0.6 to 1.26	1.46	0.4–0.51	Up to 6	N/R	No	[103]
Ellipsoid	0.4–0.8	~1.63 to 3.25	1.458	0.72–0.78	Up to 28.9	N/R	No	[104]
Dome-shaped fiber tip	1.064	~28 to 103	$n_c = 1.44$, $n_{cl} = 1.457$	~0.94 to 3.95	Up to 4.63	N/R	No	[105]
Fiber-coupled spheroid	0.6328	~7	1.43–1.59	N/R	~26 to 40	N/R	No	[106]

Table 1. Characteristics of photonic jets produced by objects with various shapes and sizes. *DS* Dirac semi-metal, *LC* liquid crystal, *N/R* Not reported, n_c core index, n_s shell index, n_{cl} cladding index.

Data availability
The datasets used and/or analyzed during the current study are available from the corresponding author on reasonable request.

References

1. Chen, Z., Taflove, A. & Backman, V. Photonic nanojet enhancement of backscattering of light by nanoparticles: a potential novel visible-light ultramicroscopy technique. *Opt. Express* **12**(7), 1214–1220 (2004).
2. Darafsheh, A. Photonic nanojets and their applications. *J. Phys. Photon.* **3**(2), 022001 (2021).
3. Lukyanchuk, B. S., Paniagua-Domínguez, R., Minin, I., Minin, O. & Wang, Z. "Refractive index less than two: photonic nanojets yesterday, today and tomorrow [Invited]. *Optical Materials Express* **7**(6), 1820–1847 (2017).
4. Gu, G., Zhang, P., Chen, S., Zhang, Y. & Yang, H. Inflection point: a perspective on photonic nanojets. *Photon. Res.* **9**(7), 1157–1171 (2021).
5. I. Minin and O. Minin, "Photonic jets formation by non spherical axially and spatially asymmetric 3D dielectric particles," in *Diffractive Optics and Nanophotonics* by I. Minin and O. Minin (Springer, Heidelberg), 31–54 (2015).

6. Pacheco-Peña, V. & Beruete, M. Photonic nanojets with mesoscale high-index dielectric particles. *Journal of Applied Physics* **125**(8), 084104 (2019).
7. Mendes, M. J., Tobías, I., Martí, A. & Luque, A. Near-field scattering by dielectric spheroidal particles with sizes on the order of the illuminating wavelength. *J. Opt. Soc. Am. B* **27**(6), 1221–1231 (2010).
8. Liu, C.-Y. Photonic jets produced by dielectric micro cuboids. *Appl. Optics* **54**(29), 8694–8699 (2015).
9. Pacheco-Peña, V., Beruete, M., Minin, I. V. & Minin, O. V. Terajets produced by dielectric cuboids. *Appl. Phys. Lett.* **105**(8), 084102 (2014).
10. Geints, Y. E., Zemlyanov, A. A. & Panina, E. K. Microaxicon-generated photonic nanojets. *Journal of the Optical Society of America B* **32**(8), 1570–1574 (2015).
11. Minin, I. V., Liu, C. Y., Geints, Y. E. & Minin, O. V. Recent advances in integrated photonic jet-based photonics. *Photonics* **7**(2), 41 (2020).
12. Liu, C.-Y., Minin, O. V. & Minin, I. V. First experimental observation of array of photonic jets from saw-tooth phase diffraction grating. *EPL (Europhysics Letters)* **123**(5), 54003 (2018).
13. Minin, I. V., Minin, O. V. & Geints, Y. E. Localized EM and photonic jets from non-spherical and non-symmetrical dielectric mesoscale objects: Brief review. *Annalen der Physik* **527**(7–8), 491–497 (2015).
14. Han, L., Han, Y., Gouesbet, G., Wang, J. & Gréhan, G. Photonic jet generated by spheroidal particle with Gaussian-beam illumination. *J. Opt. Soc. Am. B* **31**(7), 1476–1483 (2014).
15. Jia, Y., Li, R., Zhuang, W. & Liang, J. Photonic nanojet generated by a spheroidal particle illuminated by a vector Bessel beam. *Results in Optics* **4**, 100106 (2021).
16. Darafsheh, A. Microsphere-assisted microscopy. *J. Appl. Phys.* **131**(3), 031102 (2022).
17. Darafsheh, A., Guardiola, C., Palovcak, A., Finlay, J. C. & Carabe, A. Optical super-resolution imaging by high-index microspheres embedded in elastomers. *Optics Letters* **40**(1), 5–8 (2015).
18. Darafsheh, A. Optical super-resolution and periodical focusing effects by dielectric microspheres, Ph.D. dissertation (University of North Carolina at Charlotte, 2013).
19. Darafsheh, A. Comment on 'Super-resolution microscopy by movable thin-films with embedded microspheres: Resolution analysis' [Ann. Phys. (Berlin) 527, 513 (2015)]. *Ann. Phys. (Berlin)* **528**(11–12), 898–900 (2016).
20. Alessandri, I. & Lombardi, J. R. Enhanced Raman scattering with dielectrics. *Chem. Rev.* **116**(24), 14921–14981 (2016).
21. Darafsheh, A. & Abbasian, V. Dielectric microspheres enhance microscopy resolution mainly due to increasing the effective numerical aperture. *Light Sci. Appl.* **12**(1), 22 (2023).
22. Hüser, L., Pahl, T., Künne, M. & Lehmann, P. Microsphere assistance in interference microscopy with high numerical aperture objective lenses. *J. Opt. Microsyst.* **2**(4), 044501 (2022).
23. T. Pahl, L. Hüser, S. Hagemeier, and P. Lehmann, "FEM-based modeling of microsphere-enhanced interferometry," Light: Advanced Manufacturing, 3, 49 (2022).
24. Abbasian, V., Darafsheh, A. & Moradi, A.-R. Simple high-resolution 3D microscopy by a dielectric microsphere: a proof of concept. *Optics Letters* **48**(23), 6216–6219 (2023).
25. Li, Y., Qian, J., Feng, S., Chen, Q. & Zuo, C. Deep-learning-enabled dual-frequency composite fringe projection profilometry for single-shot absolute 3D shape measurement. *Opto-Electron. Adv.* **5**(5), 210021 (2022).
26. Darafsheh, A. & Abbasian, V. Microsphere-assisted microscopy: challenges and opportunities. *Proceedings of SPIE* **12618**, 126180L (2023).
27. Abbasian, V. *et al.* Microsphere-assisted quantitative phase microscopy: A review. *Light Adv. Manuf.* **5**, 6 (2024).
28. Jacassi, A. *et al.* Scanning probe photonic nanojet lithography. *ACS Appl. Mater. Interfaces* **9**(37), 32386–32393 (2017).
29. Bonakdar, A. *et al.* Deep-UV microsphere projection lithography. *Optics Letters* **40**(11), 2537–2540 (2015).
30. Wang, H., Wu, X. & Shen, D. Trapping and manipulating nanoparticles in photonic nanojets. *Opt. Lett.* **41**(7), 1652–1655 (2016).
31. Darafsheh, A. & Astratov, V. N. Periodically focused modes in chains of dielectric spheres. *Appl. Phys. Lett.* **100**(6), 61123 (2012).
32. Darafsheh, A. *et al.* Formation of polarized beams in chains of dielectric spheres and cylinders. *Optics Lett.* **38**(20), 4208–4211 (2013).
33. Allen, K. W. *et al.* Microsphere-chain waveguides: Focusing and transport properties. *Appl. Phys. Lett.* **105**(2), 021112 (2014).
34. Zhang, Y., He, Y., Wang, H., Sun, L. & Su, Y. Ultra-broadband mode size converter using on-chip metamaterial-based Luneburg lens. *ACS Photon.* **8**(1), 202–208 (2021).
35. Darafsheh, A. *et al.* Contact focusing multimodal microprobes for ultraprecise laser tissue surgery. *Optics Express* **19**(4), 3440–3448 (2011).
36. Hutchens, T. C. *et al.* Detachable microsphere scalpel tips for potential use in ophthalmic surgery with the erbium:YAG laser. *J. Biomed. Opt.* **19**(1), 18003 (2014).
37. Abbasian, V. & Darafsheh, A. A dataset of digital holograms of normal and thalassemic cells. *Sci. Data* **11**, 3 (2024).
38. Minin, I. V., Minin, O. V., Pacheco-Peña, V. & Beruete, M. All-dielectric periodic terajet waveguide using an array of coupled cuboids. *Appl. Phys. Lett.* **106**(5), 254102 (2015).
39. Minin, I. V., Minin, O. V., Pacheco-Peña, V. & Beruete, M. Localized photonic jets from flat, three-dimensional dielectric cuboids in the reflection mode. *Optics Lett.* **40**(10), 2329–2332 (2015).
40. Pham, H. H. N., Hisatake, S., Minin, I. V., Minin, O. V. & Nagatsuma, T. Three-dimensional direct observation of Gouy phase shift in a terajet produced by a dielectric cuboid. *Appl. Phys. Lett.* **108**(19), 191102 (2016).
41. Pacheco-Peña, V., Beruete, M., Minin, I. V. & Minin, O. V. Multifrequency focusing and wide angular scanning of terajets. *Optics Lett.* **40**(2), 245–248 (2015).
42. Minin, I. V. & Minin, O. V. Ultrafast all-optical THz modulation based on wavelength scaled dielectric particle with graphene monolayer. *Proc. SPIE* **11065**, 110651J (2019).
43. Minin, I. V. *et al.* Responsivity enhancement of a strained silicon field-effect transistor detector at 0.3 THz using the terajet effect. *Optics Lett.* **46**(13), 3061–3064 (2021).
44. Pawar, A. Y., Sonawane, D. D., Erande, K. B. & Derle, D. V. Terahertz technology and its applications. *Drug Invention Today* **5**(2), 157–163 (2013).
45. Nguyen Pham, H. H., Hisatake, S., Minin, O. V., Nagatsuma, T. & Minin, I. V. Enhancement of spatial resolution of terahertz imaging systems based on terajet generation by dielectric cube. *APL Photon.* **2**(5), 056106 (2017).
46. Hu, X., Zhou, L., Wu, X. & Peng, Y. Review on near-field detection technology in the biomedical field. *Adv. Photon. Nexus* **2**(4), 044002 (2023).
47. Chen, X. *et al.* Terahertz (THz) biophotonics technology: instrumentation, techniques, and biomedical applications. *Chem. Phys. Rev.* **3**, 011311 (2022).
48. Shen, S. *et al.* Recent advances in the development of materials for terahertz metamaterial sensing. *Adv. Opt. Mater.* **10**, 2101008 (2022).
49. Jahn, D. *et al.* Digital aerosol jet printing for the fabrication of terahertz metamaterials. *Adv. Mater. Technol.* **3**(2), 1700236 (2018).
50. Chopra, N., Deveikis, J. & Lloyd-Hughes, J. Active THz beam shaping using a one-dimensional array of photoconductive emitters. *Appl. Phys. Lett.* **122**(6), 061102 (2023).
51. Herter, A. *et al.* Terahertz waveform synthesis in integrated thin-film lithium niobate platform. *Nat. Commun.* **14**, 11 (2023).

52. Darafsheh, A. & Bollinger, D. Systematic study of the characteristics of the photonic nanojets formed by dielectric microcylinders. *Optics Commun.* **402**, 270–275 (2017).
53. Lecler, S., Takakura, Y. & Meyrueis, P. Properties of a three-dimensional photonic jet. *Optics Lett.* **30**(19), 2641–2643 (2005).
54. Li, X., Chen, Z., Taflove, A. & Backman, V. Optical analysis of nanoparticles via enhanced backscattering facilitated by 3-D photonic nanojets. *Opt. Express* **13**(2), 526–533 (2005).
55. Geints, Y. E., Zemlyanov, A. A., Minin, O. V. & Minin, I. V. Systematic study and comparison of photonic nanojets produced by dielectric microparticles in 2D- and 3D-spatial configurations. *J. Opt.* **20**, 065606 (2018).
56. Darafsheh, A. Influence of the background medium on imaging performance of microsphere-assisted super-resolution microscopy. *Optics Lett.* **42**(4), 735–738 (2017).
57. Mandal, A., Tiwari, P., Upputuri, P. K. & Dantham, V. R. Characteristic parameters of photonic nanojets of single dielectric microspheres illuminated by focused broadband radiation. *Sci. Rep.* **12**, 173 (2022).
58. Geints, Y. E., Panina, E. K. & Zemlyanov, A. A. Control over parameters of photonic nanojets of dielectric microspheres. *Optics Commun.* **283**, 4775–4781 (2010).
59. Wang, Y.-J., Dai, C.-A. & Li, J.-H. Numerical study of tunable photonic nanojets generated by biocompatible hydrogel core-shell microspheres for surface-enhanced raman scattering applications. *Polymers* **11**(3), 431 (2019).
60. Liu, C. Y. Tunable nanojet-induced mode achieved by coupled core–shell microcylinders with nematic liquid crystals. *Optics Commun.* **378**(3), 229–234 (2014).
61. Eti, N., Giden, I. H., Hayran, Z., Rezaei, B. & Kurt, H. Manipulation of photonic nanojet using liquid crystals for elliptical and circular core-shell variations. *J. Mod. Opt.* **64**(15), 1566–1577 (2017).
62. Soh, J. H., Wu, M., Gu, G., Chen, L. & Hong, M. Temperature-controlled photonic nanojet via VO_2 coating. *Appl. Opt.* **55**(14), 3751–3756 (2016).
63. Dukhopelnykov, S. V., Sauleau, R., Garcia-Vigueras, M. & Nosich, A. I. Combined plasmon-resonance and photonic-jet effect in the THz wave scattering by dielectric rod decorated with graphene strip. *J. Appl. Phys.* **126**(2), 023104 (2019).
64. Masyukov, M. S. & Grebenchukov, A. N. Temporally modulated metamaterial based on a multilayer graphene structure. *Phys. Rev. B* **104**, 165308 (2021).
65. Zou, J., Yang, Z., Mao, C. & Wu, S.-T. Fast-response liquid crystals for 6G optical communications. *Crystals* **11**(7), 797 (2021).
66. Ooi, K. J. A. *et al.* Nonlinear plasmonics of three-dimensional Dirac semimetals. *APL Photonics* **4**, 034402 (2019).
67. Kotov, O. V. & Lozovik, Y. E. Dielectric response and novel electromagnetic modes in three-dimensional Dirac semimetal films. *Phys. Review B* **93**, 235417 (2016).
68. Liu, Z. K. *et al.* Discovery of a three-dimensional topological Dirac semimetal, Na_3Bi. *Science* **343**(6173), 864–867 (2014).
69. Liu, G.-D. *et al.* Dirac semimetals based tunable narrowband absorber at terahertz frequencies. *Optics Express* **26**(9), 11471–11480 (2018).
70. Shen, Q. & Xiong, H. An amplitude and frequency tunable terahertz absorber. *Results in Physics* **34**, 105263 (2022).
71. Xiong, H., Ma, X. & Zhang, H. Wave-thermal effect of a temperature-tunable terahertz absorber. *Optics Express* **29**(23), 38557–38566 (2021).
72. Wang, Q.-G., Gao, B., Wu, G., Tian, X.-J. & Liu, L. Tunable dual-spectral plasmon-induced transparency in terahertz Dirac semimetal metamaterials. *Microw. Opt. Technol. Lett.* **65**(5), 1448–1455 (2023).
73. Armitage, N. P., Mele, E. J. & Vishwanath, A. Weyl and Dirac semimetals in three-dimensional solids. *Rev. Mod. Phys.* **90**, 015001 (2018).
74. Wang, L.-X., Li, C.-Z., Yu, D.-P. & Liao, Z.-M. Aharonov-Bohm oscillation in Dirac semimetal Cd_3As_2 nanowires. *Nat. Commun.* **7**, 10769 (2016).
75. Li, Z. *et al.* Active manipulation of Dirac semimetals supported chiral coding metasurfaces for multifunctional applications in terahertz region. *Results Phys.* **46**, 106323 (2023).
76. Thareja, V. *et al.* Electrically tunable coherent optical absorption in graphene with ion gel. *Nano Lett.* **15**(3), 1570–1576 (2015).
77. Weber, C. P. Ultrafast investigation and control of Dirac and Weyl semimetals. *J. Appl. Phys.* **129**(7), 070901 (2021).
78. Wang, Q. *et al.* Ultrafast broadband photodetectors based on three-dimensional Dirac semimetal Cd_3As_2. *Nano Lett.* **17**(2), 834–841 (2017).
79. Yahyapour, B. & Rezaei, B. Generation of tunable terajet via a dielectric rod covered with Dirac semimetal. *J. Appl. Phys.* **130**(8), 083103 (2021).
80. Lee, Y.-S. *Principles of Terahertz Science and Technology* (Springer, 2009).
81. Berenger, J.-P. A perfectly matched layer for the absorption of electromagnetic waves. *J. Comput. Phys.* **114**(2), 185–200 (1994).
82. Crassee, I., Sankar, R., Lee, W.-L., Akrap, A. & Orlita, M. 3D Dirac semimetal Cd3As2: A review of material properties. *Phys. Rev. Mater.* **2**, 120302 (2018).
83. Li, R. *et al.* Topological metal of NaBi with ultralow lattice thermal conductivity and electron-phonon superconductivity. *Sci. Reports* **5**, 8446 (2015).
84. Zhou, R. *et al.* Recent advances in photonics of threedimensional Dirac semimetal Cd_3As_2. *Adv. Photon. Nexus* **1**(2), 024001 (2022).
85. Li, C.-Z. *et al.* Synthesis and photovoltaic properties of Cd_3As_2 faceted nanoplates and nano-octahedrons. *Crystal Growth Design* **15**(7), 3264–3270 (2015).
86. Uchida, M. *et al.* Quantum Hall states observed in thin films of Dirac semimetal Cd_3As_2. *Nat. Commun.* **8**, 2274 (2017).
87. Yang, M. *et al.* Ultraviolet to long-wave infrared photodetectors based on a three-dimensional Dirac semimetal/organic thin film heterojunction. *J. Phys. Chem. Lett.* **10**(14), 3914–3921 (2019).
88. Zhang, K. *et al.* Controllable synthesis and magnetotransport properties of Cd_3As_2 Dirac semimetal nanostructures. *RCS Adv.* **7**, 17689 (2017).
89. Liu, Y. *et al.* Gate-tunable quantum oscillations in ambipolar Cd_3AS_2 thin films. *NPG Asia Mater.* **7**, e221 (2015).
90. Nishihaya, S. *et al.* Gate-tuned quantum Hall states in Dirac semimetal $(Cd_{1-x}Zn_x)_3As_2$. *Sci. Adv.* **4**(5), 566 (2018).
91. Shoron, O. F., Schumann, T., Goyal, M., Kealhofer, D. A. & Stemmer, S. Field-effect transistors with the three-dimension Dirac semimetal cadmium arsenide. *Appl. Phys. Lett.* **115**(6), 062101 (2019).
92. Cheng, B. *et al.* Efficient terahertz harmonic generation with coherent acceleration of electrons in the Dirac semimetal Cd_3As_2. *Phys. Rev. Lett.* **124**, 117402 (2020).
93. Liu, Z. K. *et al.* A stable three-dimensional topological Dirac semimetal Cd_3As_2. *Nat. Mater.* **13**, 677–681 (2014).
94. Zhou, S. Effects of light polarization in photonic nanojet. *Opt. Quant. Electron.* **51**, 112 (2019).
95. Liu, C. Y. & Lin, F. C. Geometric effect on photonic nanojet generated by dielectric microcylinders with non-cylindrical cross-sections. *Opt. Commun.* **380**, 287–296 (2016).
96. Richards, B. & Wolf, E. Electromagnetic diffraction in optical systems II, structure of the image field in an aplantic system. *Proc. R. Soc. London A* **253**(1274), 358–379 (1959).
97. Geints, Y. E., Zemlyanov, A. A. & Panina, E. K. Photonic jets from resonantly excited transparent dielectric microspheres. *J. Opt. Soc. Am. B* **29**(4), 758–762 (2012).
98. Kotlyar, V. V. & Stafeev, S. S. Modeling the sharp focus of a radially polarized laser mode using a conical and a binary microaxicon. *J. Opt. Soc. Am. B* **27**(10), 1991–1997 (2010).

99. V. D. Zaitsev and S. S. Stafeev, Photonic jets arrays produced by triangular dielectric prisms for mid-IR imaging. In 2019 PhotonIcs & Electromagnetics Research Symposium - Spring (PIERS-Spring), 2610–2614 (2019).

100. Wang, H., Zhou, X., Chen, X. & Han, Y. Tunable terajets formed by core-shell microspheres for high-resolution terahertz zoom imaging. *Proc. SPIE* **12935**, 129351U (2023).

101. Hengyu, Z., Zaichun, C., Chong, C. T. & Minghui, H. Photonic jet with ultralong working distance by hemispheric shell. *Optics Express* **23**(5), 6626–6633 (2015).

102. Liu, X. *et al.* Photonic nanojets with ultralong working distance and narrowed beam waist by immersed engineered dielectric hemisphere. *Optics Express* **28**(23), 33959–33970 (2020).

103. Stafeev, S. S. & Kotlyar, V. V. Measurement of photonic nanojet generated by square-profile microstep. *Proc. SPIE* **9448**, 94482C (2015).

104. Wei, B. *et al.* Photonic jet generated by a dielectric ellipsoidal particle. *J. Quant. Spectrosc. Radiat. Transf.* **242**, 106786 (2020).

105. Bouaziz, D., Chabrol, G., Guessoum, A., Demagh, N.-E. & Lecler, S. Photonic jet-shaped optical fiber tips versus lensed fibers. *Photonics* **8**(9), 373 (2021).

106. Han, L., Han, Y., Wang, J., Gouesbet, G. & Gréhan, G. Controllable and enhanced photonic jet generated by fiber combined with spheroid. *Opt. Lett.* **39**(6), 1585–1588 (2014).

Author contributions

B. Yahyapour performed the simulations. All authors have participated in conception and design, analysis and interpretation of the data, drafting the manuscript and approval of the final version.

Competing interests

The authors declare that they have no competing financial interests or personal relationships that could have appeared to influence the work reported in this manuscript.

Additional information

Correspondence and requests for materials should be addressed to B.R.

Reprints and permissions information is available at www.nature.com/reprints.

Publisher's note Springer Nature remains neutral with regard to jurisdictional claims in published maps and institutional affiliations.